RESEARCH ARTICLE

Key Points:
- Ion energy flux enhancement at several keV to tens of keV is observed inside foreshock transients cores indicating ion acceleration
- We reveal that one ion acceleration mechanism is reflection at the earthward moving boundary of foreshock transients
- Three-dimensional global hybrid simulation is employed to confirm our observation results

Ion Acceleration Inside Foreshock Transients

Terry Z. Liu[1] iD**, San Lu[1]** iD**, Vassilis Angelopoulos[1], Yu Lin[2]** iD**, and X. Y. Wang[2]** iD

[1]Department of Earth, Planetary, and Space Sciences and Institute of Geophysics and Planetary Physics, University of California, Los Angeles, CA, USA, [2]Physics Department, Auburn University, Auburn, AL, USA

Abstract Recent observations upstream of Earth's bow shock have revealed that foreshock transients can not only accelerate solar wind ions by reflection at their upstream boundaries but may also accelerate ions inside them. Evidence for the latter comes from comparisons of ion spectra inside and outside the cores, and from evidence of leakage of suprathermal ions from the cores. However, definite evidence for, and the physics of, ion acceleration in the foreshock transients are still open questions. Using case studies of foreshock transients from Time History of Events and Macroscale Interactions during Substorms observations, we reveal an ion acceleration mechanism in foreshock transients that is applicable to ~25% of the transients. The ion energy flux is enhanced between several keV to tens of keV in the cores. We show that these energetic ions are reflected at the earthward moving boundary of foreshock transients, are accelerated through partial gyration along the convection electric field, and can leak out both upstream and downstream of the foreshock transients. Using ions moving self-consistently with a generic 3-D global hybrid simulation of a foreshock transient, we confirm this physical picture of ion acceleration and leakage. These accelerated ions could be further accelerated at the local bow shock and repopulate the foreshock, increasing the efficacy of solar wind-magnetosphere interactions.

1. Introduction

Earth's foreshock is filled with backstreaming particles reflected and accelerated at the bow shock (e.g., Eastwood et al., 2005). Under certain conditions, mostly during a Sun-Earth-aligned solar wind magnetic field, these particles can interact with solar wind plasma and discontinuities, forming many types of foreshock transients. These include foreshock bubbles (FBs) (Liu et al., 2015; Omidi et al., 2010; Turner et al., 2013), hot flow anomalies (HFAs) (e.g., Lin, 2002; Omidi & Sibeck, 2007; Schwartz et al., 1985), spontaneous hot flow anomalies (SHFAs) (Omidi et al., 2013; Zhang et al., 2013), and foreshock cavities (e.g., Lin, 2003; Sibeck et al., 2002). Foreshock bubbles and hot flow anomalies form from concentration and thermalization of foreshock ions at a solar wind discontinuity as the resulting enhanced thermal pressure pushes back on surrounding cold solar wind ions. Spontaneous hot flow anomalies look similar to hot flow anomalies, but form due to the interaction between foreshock cavitons (e.g., Blanco-Cano et al., 2011) and the bow shock spontaneously without discontinuities. Foreshock cavities form when a foreshock region is bounded by field lines that are unconnected to the bow shock, which results in pressure difference and expansion (Schwartz et al., 2006). These four types of foreshock transients have a common characteristic: a hot, tenuous core surrounded by a shock or compressional boundaries. Because of the low dynamic pressure in their cores, as they encounter the bow shock they cause it to move outward, resulting in perturbations in the magnetosphere-ionosphere system (e.g., Archer et al., 2014, 2015; Sibeck et al., 1999).

Recent observations have revealed another important aspect of these foreshock transients, particle acceleration (e.g., Kis et al., 2013; Liu, Hietala, et al., 2016; Wilson et al., 2013, 2016). Although shock acceleration is one of the most important acceleration mechanisms in the universe, the physical mechanism behind such highly effective acceleration is still not fully understood. For example, the energetic particle source for diffusive shock acceleration is unclear (this is also known as the injection problem (e.g., Caprioli et al., 2015; Jokipii, 1987; Sundberg et al., 2016)). Recent observations (e.g., Liu, Hietala, et al., 2016; Wilson et al., 2016) suggest that foreshock transients may be an efficient preaccelerator of particles for the parent shock, and they may work synergistically with other shock acceleration processes at the most potent shocks. Therefore, it is important to understand how foreshock transients accelerate particles.

Recent observations have revealed several mechanisms of particle acceleration by foreshock transients. Because foreshock bubbles typically expand faster than the local fast-wave speed (e.g., Liu, Turner, et al., 2016), a

new shock (the FB shock) forms upstream of the core. Like Earth's bow shock, an FB shock can reflect and accelerate solar wind particles through shock drift acceleration, forming a new foreshock, the FB foreshock (Liu, Hietala, et al., 2016). Additionally, inside foreshock transients' cores, electrons can be accelerated to hundreds of keV (Wilson et al., 2016). A recent statistical study revealed that almost all foreshock transients (including FBs, HFAs, SHFAs, and possibly foreshock cavities) can accelerate electrons in their cores (Liu, Angelopoulos, Hietala, & Wilson, 2017). Fermi acceleration, that is, bouncing between the converging bow shock and foreshock transient's boundary, is one of the acceleration mechanisms (Liu, Lu, et al., 2017).

Ion mean energy enhancement in foreshock transients' cores, on the other hand, has been observed clearly only occasionally in a recent statistical study (Liu, Angelopoulos, Hietala, & Wilson, 2017). However, as pointed out in that study, energetic ions accelerated in the foreshock transients have gyroradii that are very much larger than foreshock transient boundaries, and thus, some of these ions can readily escape from the core to the solar wind (see section 5 for detailed discussion). Such escape was clearly documented in Liu, Angelopoulos, and Hietala (2017). Therefore, ion leakage from the core into the region surrounding foreshock transients can mask our detection of ion acceleration in foreshock transients by lowering the ion flux and average energy in the core and enhancing them in the background. This implies that ion acceleration in foreshock transients can evade detection and thus may be more common than surmised from earlier statistics. How common ion acceleration is inside foreshock transients, definitive observational evidence for the ion acceleration process there, and the physics of the acceleration mechanism are still open questions.

Previous 2-D hybrid simulations by Omidi et al. (2010) suggest that ions may be accelerated by bouncing between the bow shock and an earthward moving FB's upstream boundary, which could also be true for HFAs, SHFAs, and foreshock cavities, although this effect has not been reported observationally. Electrons, however, have been recently observed to be accelerated through such a process (clearly, in a small subset, 13%, of electron acceleration events; the process may also be operational in other cases but may be more difficult to prove in those cases) (Liu, Lu, et al., 2017). Therefore, it is reasonable to hypothesize that a similar, Fermi-like process also operates on ions.

To find evidence for this process, we perform case studies using Time History of Events and Macroscale Interactions during Substorms (THEMIS) data. To further confirm our observational results and our understanding of the acceleration process, we also apply global hybrid simulations and particle tracing. In 2-D simulations a foreshock bubble is infinitely long in the third dimension, meaning that ions are more easily trapped inside an FB. Thus, in 2-D simulations, ions are more likely to bounce at the approaching boundaries before escaping than in reality, because FBs are finite in all three dimensions. Therefore, here we employ 3-D hybrid simulations to achieve a more realistic, finite FB spatial structure.

An overview of our data and simulation approach will be presented in section 2. We will show three observational case studies in section 3. Simulation results and their comparison to observations will be presented in section 4. In section 5 we will discuss our results and potential effects. We summarize and conclude in section 6.

2. Data and Methods

We used data from the THEMIS mission probes TH-B and TH-C in 2008 and 2009 (Angelopoulos, 2008). In the first two dayside seasons of that mission (Sibeck & Angelopoulos, 2008), TH-B (~30 R_E apogee) and TH-C (~20 R_E apogee) were often in the foreshock. We analyzed plasma data from the electrostatic analyzer (ESA) (McFadden et al., 2008) and the solid-state telescope (SST) (Angelopoulos, 2008) and magnetic field data from the fluxgate magnetometer (Auster et al., 2008). In this work, other than GSE coordinates, DSL phi is also used to indicate the particles' direction of motion. In the "Despun-Sun-Lvector" (DSL) coordinate system, the Z axis is along the spacecraft's spin axis (approximately along ecliptic south) and the Y axis is the cross product between the Sun direction and Z. The third axis, X, completes the right-hand system and thus points roughly sunward. The azimuth in DSL expressed in polar coordinates, DSL phi, is roughly the reverse of GSE phi, since the spacecraft's spin axis is roughly opposite GSE Z (DSL phi = 0°, 90°, 180°, and 270° are roughly sunward, dawnward, tailward, and duskward moving particles) (Angelopoulos, 2008).

Next, we introduce how we select events. According to the simulation by Omidi et al. (2010), if ions can gain energy through bouncing, that is, reflection at the earthward moving upstream boundary of foreshock transients, earthward ions faster than the solar wind should be observed. Thus, we use the observations of energetic earthward component inside cores of foreshock transients as a criterion to search the event list of FBs, HFAs, SHFAs, and possible foreshock cavities observed in fast-survey mode in 2008 and 2009 reported in Liu, Angelopoulos, Hietala, and Wilson (2017), and we found 63 events out of 247. To further investigate whether this is caused by bouncing, we selected 13 events with less diffuse (more beam-like) ion distributions so we can more easily identify the solar wind beam, a sunward foreshock ion beam, and an earthward high-speed beam. In the next section, we present three representative events from this group.

In this study, we employ a 3-D hybrid simulation to compare with our observations. A detailed description of this code can be found in Lin and Wang (2005). The simulation is in GSE coordinates same as observations and its domain contains a hemispherical plasma region with GSE $x > 0$. In this hybrid code, the particle ions are advanced by their equation of motion. In addition to the particle ions, a cold, incompressible ion fluid is also included in the inner magnetosphere to represent the plasmasphere. The electric field is calculated from the electron momentum equation in which the electron flow velocity is derived from Ampere's Law. The magnetic field is advanced in time using Faraday's law. Quasi-neutrality is assumed in the simulation.

The simulation uses a spherical coordinate system (r, θ, ϕ) and is carried out within a geocentric distance $4 R_E < r < 25 R_E$. The initial condition includes a dipole geomagnetic field at $r < 10 R_E$ (plus a mirror dipole field) and the solar wind at $r > 10 R_E$. A solar wind rotational discontinuity (RD) is imposed to generate foreshock transients. The magnetic field of the solar wind with the RD is described by $B_x = -B_0 \cos \phi$, $B_y = B_0 \sin \phi$, $B_z = 0$, and $\phi = \phi(x) = \Delta\phi \tanh [(x - x_{RD})/w]$, where B_0 is a characteristic magnitude to normalize the magnetic fields in the simulations, x_{RD} is the x position of the RD's center, V_{RD} is the RD's propagation speed, and w is the RD's initial half-width. In this study, we choose $B_0 = 10$ nT, $x_{RD0} = 50 R_E$, $V_{RD} = 5V_A$ ($V_A = B_0 /\sqrt{\mu_0 m_i N_0}$, where $N_0 = 6$ cm^{-3} is the solar wind density in this simulation; therefore, $V_A \simeq 89$ km/s), $w = 0.25 R_E$, and $\Delta\phi = 20°$. Downstream of the RD, $B_{x0} = B_n = -0.47B_0$, $B_{y0} = -0.171B_0$, and $B_{z0} = 0$. Here B_n denotes the magnetic field along the normal direction of the RD, the x direction in this simulation. The solar wind flow speed across the RD based on the Rankine-Hugoniot relations is $V_x = -V_{RD} - V_{An} \cos \phi$, $V_y = V_{An} \sin \phi$, $V_z = 0$, where $V_{An} = (B_n/B_0)V_A$. So upstream of the RD, $V_{x0} = -5.442V_A$, $V_{y0} = -0.161V_A$, and $V_{z0} = 0$.

We use 12,000 particles per R_E^3 to represent N_0 in the solar wind. The solar wind ion inertial length is chosen to be $d_{i0} = 0.1 R_E$ (larger than the realistic value by a factor of ~6) (e.g., Lin et al., 2014; Tan et al., 2011). A total of about 3×10^8 particles is employed in a run. The grid cells are uniformly distributed in the θ and ϕ directions, with 104 and 130 grid points, respectively. In the r direction, nonuniform grid spacing is used with a higher resolution in region of interest around the bow shock. The grid size is $\Delta r \simeq d_{i0}$ in this region so the ion kinetics can be resolved by the simulation.

In the global hybrid simulations, ion motions are self-consistently solved, so we use such self-consistent particle tracing to study the ion acceleration mechanisms in the simulation. We select a time when the foreshock transient is fully formed and interacts with the solar wind ions. At the appropriate time, motivated by observations, we pick representative energetic ions in the correct location in energy and in space and tag them. Then we rerun the simulations to trace the ion trajectories and their energy evolution and determine whether our acceleration hypotheses are valid.

3. Observations

Using THEMIS data, we now show that earthward high-speed ions can be observed inside foreshock transients' cores. We demonstrate that such energetic earthward ions are caused by reflection and acceleration at the core's earthward moving upstream boundary. Shown in our previous study (Liu, Angelopoulos, & Hietala, 2017), energetic ions can leak out. Thus, it is natural to expect leakage to be observed in this study. In Events 2 and 3, we show that such energetic earthward ions are indeed accompanied by leaked ions either downstream or upstream.
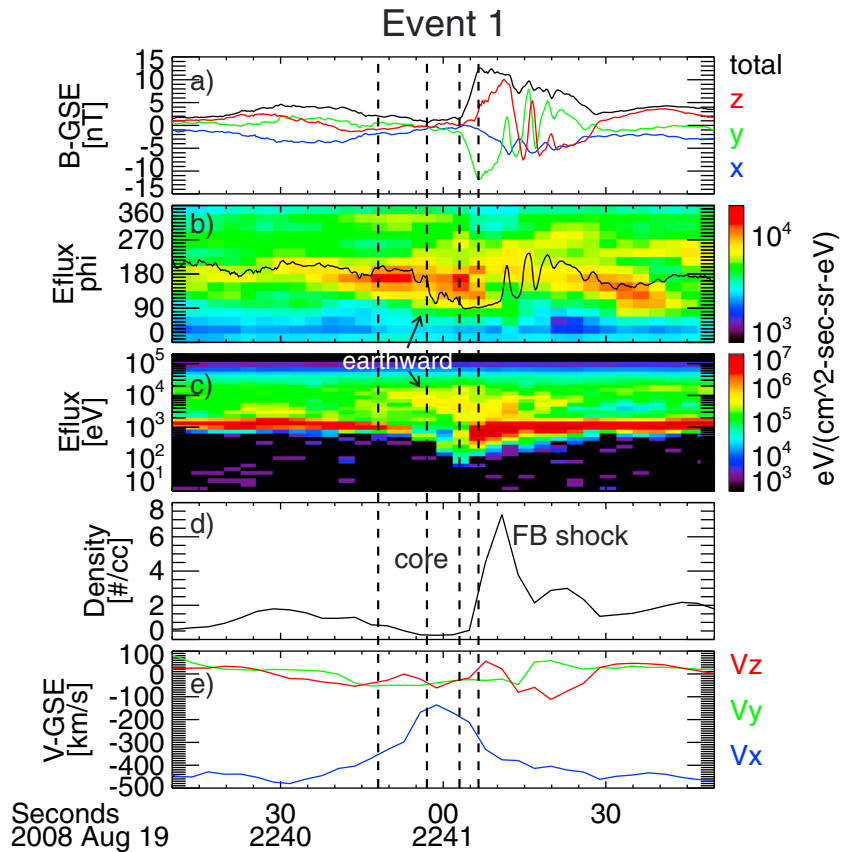
Figure 1. TH-C observations of Event 1. From top to bottom: (a) magnetic field in GSE coordinates (here and in all subsequent plots *XYZ*, total are in blue, green, red, black, respectively); (b) ion energy flux spectra in spacecraft azimuthal (phi) angle in the 50 keV to 100 keV energy range (black line indicates the magnetic field azimuth in spacecraft coordinates); (c) ion ESA and SST (combined) energy spectra; (d) total ion density; (e) ion velocity in GSE coordinates. Vertical dashed lines indicate the time of ion distributions in Figure 2.

3.1. Event 1

As shown in Figure 1, TH-C (at [15.8, 3.4, −2.7] R_E in GSE) observed a foreshock transient with a hot, tenuous core bounded by a shock-like structure on its upstream side. This foreshock transient is likely a foreshock bubble (classification of the foreshock transient type is not necessary, however). Using the magnetic/mixed-mode coplanarity method (Schwartz, 1998), we estimated the shock normal, [0.91, −0.40, −0.06]. The shock normal speed in the spacecraft frame, calculated from mass conservation (Schwartz, 1998), is ~300 km/s earthward (solar wind speed is ~520 km/s from OMNI).

Inside the core, an enhancement of ion energy flux at several keV to tens of keV can be seen in Figure 1c. The minimum energy of this energy flux enhancement gradually decreases (the ions exhibit energy dispersion). The flux enhancement, which can also be seen in the azimuthal (phi) spectra of the energy flux of 50 keV to 100 keV ions (Figure 1b), is evident mainly at 180° (earthward). Around the downstream boundary of the core (first vertical dashed line in Figure 1), this flux enhancement is along the field line (black line in Figure 1b indicates the interplanetary magnetic field (IMF) phi angle).

To fully characterize these energetic ions, we examine the ion distributions (Figure 2). Figure 2a shows the ion distribution around the downstream boundary of the core (the first vertical dashed line in Figure 1) in the *BV* plane (*X* axis is parallel to the IMF; *Y* axis is along the bulk velocity component perpendicular to the IMF). We see there are three components: the solar wind ion beam, an anti-field-aligned foreshock ion beam, and another field-aligned beam in the same direction as the solar wind but much faster (~1,000 km/s). Because the downstream IMF is mainly radial (Figure 1a), the local θ_{BN} of the bow shock is very small. Thus, as
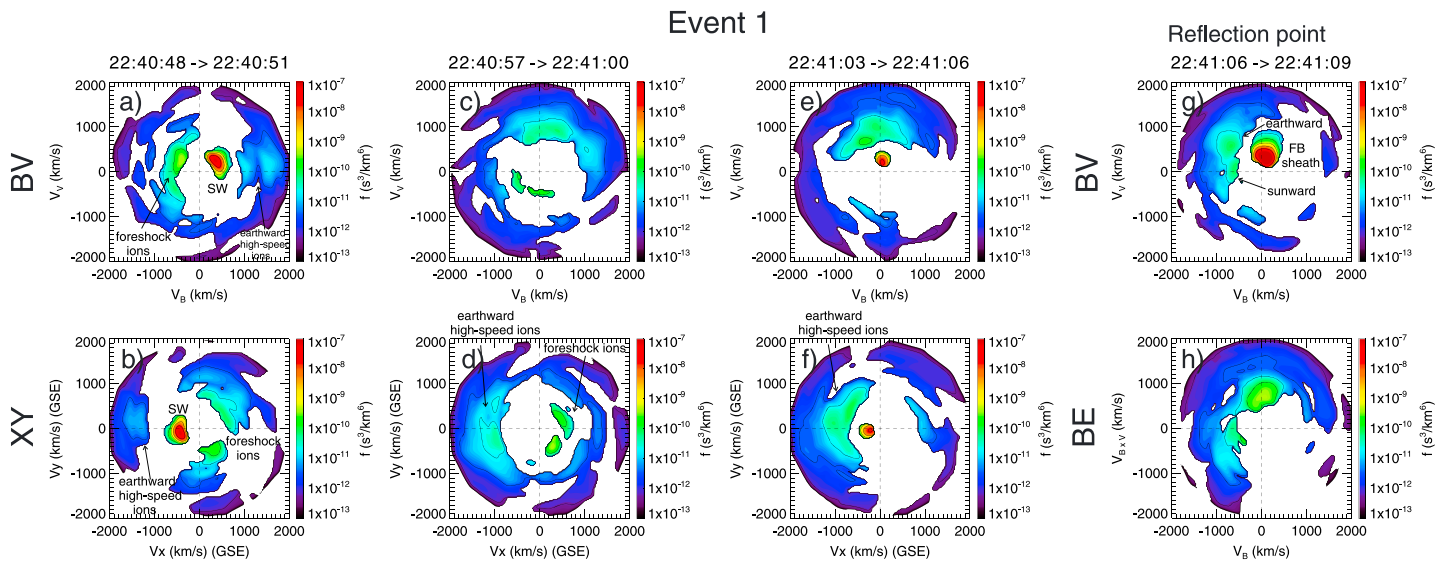
Figure 2. Ion distributions at four observation times (four columns correspond to four vertical dashed lines in Figure 1) in *BV*, GSE *XY*, and *BE* planes. The distributions are 2-D slices extracted from 3-D distributions. The *BV* plane means that the *X* axis is in the direction of the field line (averaged over 3 s) and the *V* axis is in the direction of the velocity component perpendicular to the magnetic field. The BE plane means that the *X* axis is along the field-line direction and the plane contains the convection electric field, positive along the +*Y* axis. SW is short for solar wind.

expected from adiabatic reflection model (e.g., Burgess et al., 2012), the sunward foreshock ion speed is close to the solar wind speed.

Inside the core, on the other hand, because the magnetic field is very small, the *BV* plane is not well defined. To avoid such uncertainties, we also examine the distributions in the GSE *XY* plane. In Figure 2d (middle of the core; second vertical dashed line in Figure 1), the solar wind beam is barely seen, but we can still see a sunward foreshock ion beam at ~400–500 km/s and an earthward ion beam at ~1,000 km/s. In Figure 2f, near the upstream boundary of the core (third vertical dashed line in Figure 1), the distribution is also dominated by the earthward high-speed ions. Thus, the enhancement of energy flux at several keV to tens of keV is caused by these earthward high-speed ions.

But from where do these earthward high-speed ions originate? Because the most energetic ions are moving earthward, their source should be at the upstream side of the enhancement, which is also the upstream boundary of the core (FB sheath; fourth vertical dashed line in Figure 1). Thus, one reasonable hypothesis for the ion energization is sunward foreshock ion reflection at this boundary (see sketch in Figure 3).

To analyze how these ions are reflected, we need to know the geometry of the magnetic field. In Figure 1a, the magnetic field is very small inside the core and suddenly increases to more than 10 nT at the FB sheath. Because the magnetic field is divergenceless, the magnetic field in the FB sheath near the boundary should be roughly perpendicular to the boundary normal (assumed to be the same as the FB shock normal [0.91, −0.40, −0.06]). Indeed, the magnetic field at the fourth vertical dashed line in Figure 1 has a very strong negative *Y* component and a weak negative *X* component, nearly perpendicular to the normal (or along the surface in Figure 3). When sunward ions from the core reach the FB sheath, the ion velocity must be separated into field-aligned
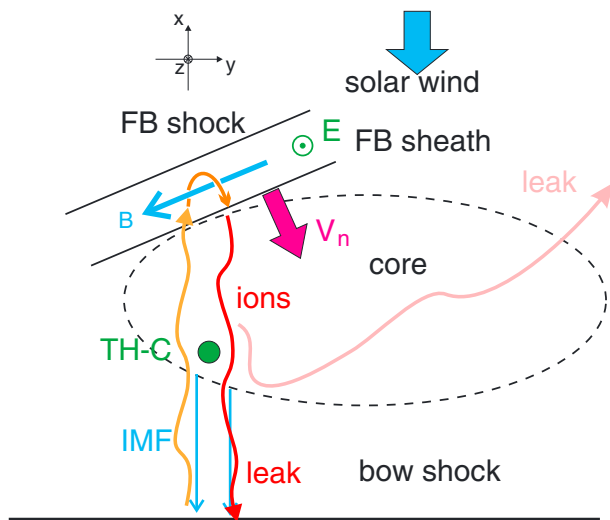

Figure 3. Sketch of Event 1. The orientation of the FB sheath and the field direction are sketched based on measurements. Solar wind ions are first reflected by the bow shock and then become sunward field-aligned foreshock ions (orange squiggly line). When these foreshock ions encounter the enhanced magnetic field at the FB sheath, they gyrate partially along the convection electric field (orange half turn) then move with higher energy/speed back toward the core and occasionally past it, earthward, toward the bow shock (red squiggly line). Some of them can also move upstream and leak out (pink squiggly line).

motion and gyromotion. Seen from the geometry in Figure 3, the field-aligned component, though determined by the injection direction of each ion, is on average opposite to the field direction. These ions can only gyrate partially, mainly along negative Z, and then move back to the core. In the spacecraft frame (Earth frame), ions gain twice the boundary normal velocity because of their partial gyration along the convection electric field (mainly in negative Z) inside the FB sheath (Figure 3), that is, specular reflection off a moving boundary.

To confirm this process, we look at the distribution function (Figures 2g and 2h) collected near the fourth vertical dashed line in Figure 1. Because the gyroradius of ions with 1–10 keV in a 10 nT field is ~1,000 km and the boundary normal speed is ~300 km/s, the distributions (each collected during a minimum accumulation time of 3 s, the spin period) can cover most of the reflecting ions. In Figure 2g (BV plane), we see that the FB sheath flow is mainly in the perpendicular direction ($E \times B$ drift, ~300 km/s earthward calculated using FB sheath velocity and 3 s averaged magnetic field) and secondary ions are antiparallel to the field. Figure 2h is the ion distribution in the BE plane (Y axis is the convection electric field direction; BE plane is perpendicular to the BV plane). We see that these ions gyrate only partially, mainly along the convection electric field (along Y axis). Therefore, the distributions are consistent with what we expect from reflection at the upstream boundary.

Next, we discuss the energy gain from this process. Note that in Figure 2g, the Y axis is approximately earthward. If transformed into the rest frame of the FB sheath flow (where the convection electric field is zero), sunward and earthward moving ions (ions before and after reflection) have roughly the same speed. However, in the spacecraft frame (Earth frame) in Figure 2g, the earthward moving (reflected) ions have an additional twice the $E \times B$ drift speed (~600 km/s) of sunward (unreflected) ions. Indeed, in Figures 2b and 2d we see that the speed difference in the x direction between sunward (~400–500 km/s) and earthward (~1000 km/s) ions is roughly 600 km/s. We conclude that these earthward high-speed ions are the ions reflected by the earthward moving boundary.

The ion energy flux enhancements in our event extend outside the core's downstream boundary (around 22:40:30–22:40:45 in Figures 1b and 1c). A previous study has shown that because of their large gyroradii, energetic ions can easily leak from the interior of foreshock transient cores into the ambient solar wind (Liu, Angelopoulos, & Hietala, 2017), and we suspect a similar phenomenon is occurring here. However, because of the large, variable background magnetic field, we cannot identify the exact location of the downstream boundary to definitively claim that downstream leakage is occurring. We will show that process next for Event 2, which does exhibit a clear downstream boundary.

3.2. Event 2

As shown in Figure 4, TH-C ([16.4, 2.7, −2.9] R_E in GSE) observed a foreshock transient with a shock-like structure on its upstream side. This foreshock transient is likely a foreshock bubble. Using the magnetic/mixed-mode coplanarity method (Schwartz, 1998), we estimated a shock normal [0.86, −0.31, 0.39]. The shock normal speed in the spacecraft frame (Earth frame) calculated from mass conservation (Schwartz, 1998) is ~130 km/s earthward (solar wind speed is ~410 km/s from OMNI).

As in Event 1, inside the core there is an enhancement of ion energy flux of about several keV to tens of keV (Figure 4c). This can also be seen in Figure 4b, where the 50 keV to 100 keV ion energy flux angular spectra show an ion enhancement, mainly in the earthward direction. Figure 5 shows ion distributions in the BV and XY planes at the three vertical dashed lines in Figure 4. As in Event 1, inside the core (Figure 5d), we see three main components: the solar wind beam, sunward foreshock ions, and earthward high-speed ions. The flux enhancement at several keV to tens of keV is mainly caused by the earthward high-speed ions, the most energetic of all the components. At the boundary of the FB sheath, where B_z dominates (Figure 4a), secondary ions are mainly moving in the positive Y direction, indicating partial gyration along the convection electric field similar to Event 1 (see Figure S1 in the supporting information). In Figure 5d, the speed difference in the X direction between sunward ions (200–300 km/s) and earthward ions (~500 km/s) is also consistent with twice the boundary normal speed (~260 km/s). Therefore, as in Event 1, the ion flux enhancement is likely caused by reflection at the earthward moving boundary.

In this event, the downstream boundary of the core is very clear (vertical dotted lines in Figure 4), unlike Event 1. In the downstream ambient foreshock, energy dispersion at several keV to tens of keV can be seen
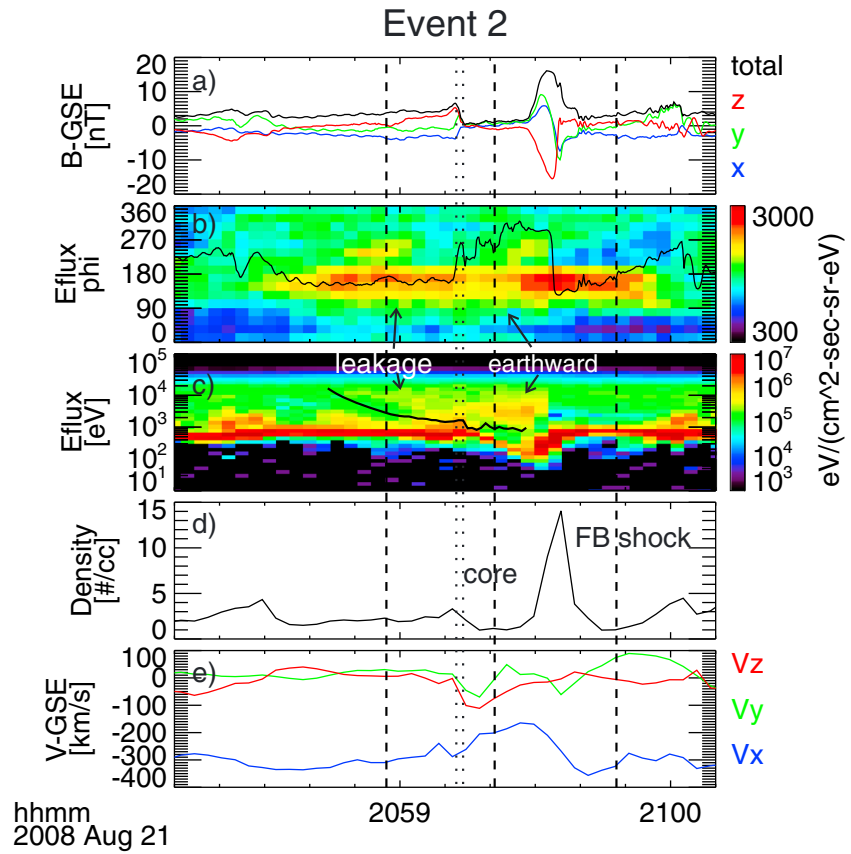
Figure 4. TH-C observations of Event 2. Same format as Figure 1. Vertical dotted lines indicate the downstream boundary of the core.
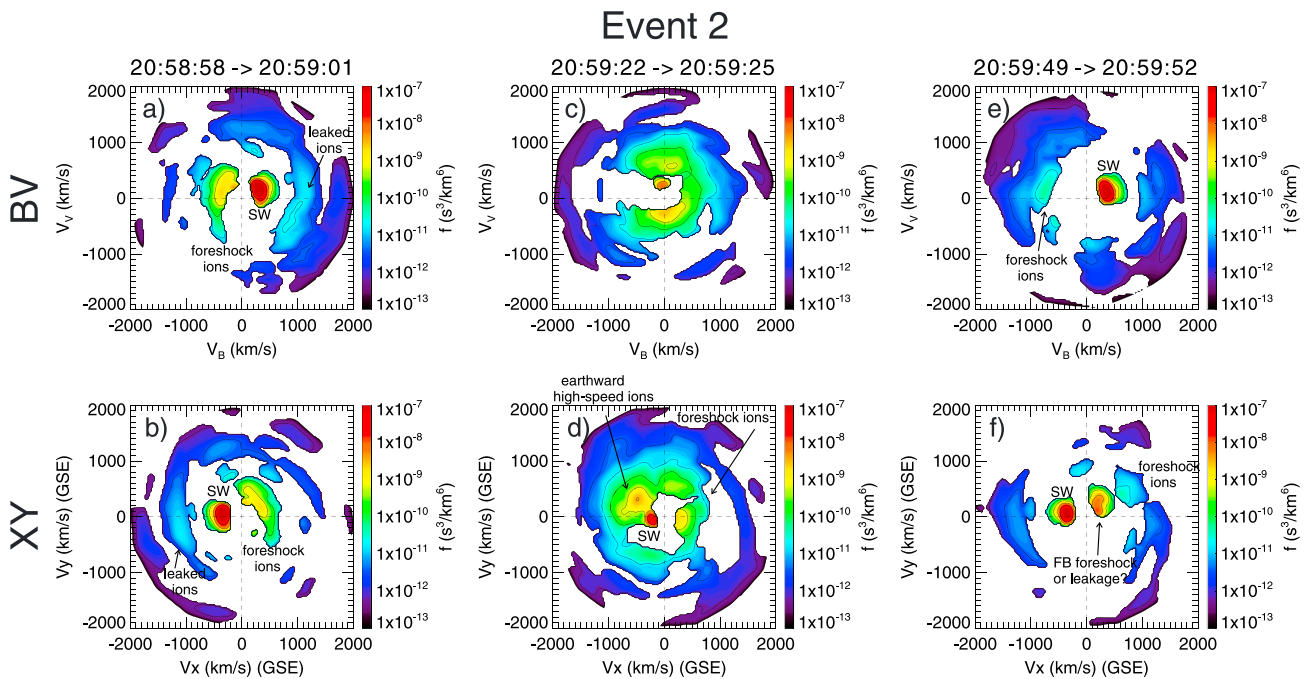

Figure 5. Ion distributions at three observation times (three columns correspond to the three vertical dashed lines in Figure 4). Format same as in Figure 2.

(Figure 4c). In the ion distributions (Figures 5a and 5b), there are three main components: the solar wind beam, a sunward anti-field-aligned foreshock ion beam, and an earthward high-speed ion beam. The foreshock ion speed is very close to the solar wind speed. Based on their elevated speed, well above that of the solar wind speed, the earthward high-speed ions correspond to the high-energy ions exhibiting dispersion in Figure 4c. Because the energy dispersion continues seamlessly into the foreshock transient and the ions were moving earthward, these ions are very likely earthward high-speed ions leaking from the core (see sketch in Figure 3).

Next, we discuss the reason for the dispersion. Using ion distributions, we have found that the dispersion is mainly caused by a decrease in parallel speed with time (and with proximity to the core). For example, at 20:58:58–20:59:01 UT the minimum parallel speed is ~800 km/s (Figure 5a); it decreases to ~700 km/s at 20:59:01–20:59:03 UT (not shown here). One possible explanation for this dispersion is that because there exists a start time for the ion source, that is, the time when ions start to be reflected toward the spacecraft once the foreshock transient forms, and because these reflected ions have different parallel speeds (as ions have broad distributions of energy and pitch angle), ions with larger parallel speed will arrive the spacecraft earlier resulting in a dispersion signature in their minimum parallel speed. (Conversely, since the ion source is continuous, there is no dispersion in the maximum parallel speed.) This model would result in a distance between the spacecraft and the source along the field line of 2–3 R_E for ions observed at 20:59:58–20:59:01 UT (estimated from $d/v_2 - d/v_1 = \Delta t$, where $v_1 = 800$ km/s, $v_2 = 700$ km/s, and $\Delta t = 3$ s). To further confirm this model, we calculate the minimum energy (the sum of minimum parallel energy and the energy from local $E \times B$ drift) as a function of time to fit the dispersion. The relation $d/v - d/v_{sw} = \Delta t$ is used to calculate the minimum parallel speed, where Δt is the observed (arrival) time difference between ions and the downstream boundary, v is ion parallel speed, and v_{sw} is solar wind speed as downstream boundary is typically the driver discontinuity convecting with the solar wind. (The reason we use downstream boundary instead of upstream boundary is that initially two boundaries are at the same position, and it is difficult to calculate the arrival time of upstream boundary due to its complicated shape and motion.) When we choose $d = $ ~2.4 R_E, the model (black line in Figure 4c) can fit the dispersion very well. Note that inside the core the minimum energy is determined by the ions moving slower than the downstream boundary; thus, the black line in the core is highly affected by the local $E \times B$ drift speed and is not very smooth. Thus, we confirm the explanation that ions with faster parallel speed arrive earlier is likely the reason of dispersion in this event and probably also in Event 1.

Next, we see if we can also identify leakage upstream. If we look at the distributions at the third vertical dashed line in Figure 4, in the *BV* plane (Figure 5e), we mainly see solar wind ions and sunward anti-field-aligned foreshock ions. In the *XY* plane (Figure 5f), on the other hand, we see there is a third component moving sunward with flux stronger than background foreshock ions. However, it is very difficult to determine whether these sunward ions are related to the FB and whether they are reflected ions by the FB shock or leaked ions from the core. In Event 3, to be discussed in the next section, there is ion leakage identified in the upstream region.

3.3. Event 3

As shown in Figure 6, TH-B ([11.9, 4.8, −2.4] R_E in GSE) observed two foreshock transients. Based on their density variations (Figure 6d), these two foreshock transients are very likely HFAs with two compressional boundaries. Their upstream boundary may be a shock, but because there is no stable upstream region for the first HFA's shock, we only calculate the normal and normal speed of the second HFA's shock: [0.89, 0.28, −0.36] and ~100 km/s earthward (solar wind speed is ~420 km/s from OMNI). Inside the cores of two foreshock transients, ion energy is higher than in the downstream background based on energy spectra (Figure 6c). Upstream of both foreshock transients, clear energy dispersion can be seen.

To further explain the ion spectra, we look at the ion distributions. Inside the cores of both foreshock transients, there are three components: solar wind ions, sunward foreshock ions, and earthward high-speed component (Figures 7a, 7b, 7e, and 7f). As in the previous two events, these are very likely ions reflected by the compressional boundary, which was moving towards the spacecraft.

Upstream of the two foreshock transients, there are only two components, a solar wind ion beam and a field-aligned component moving earthward at the $E \times B$ drift speed (Figures 7c, 7d, 7g, and 7h). First, note that the
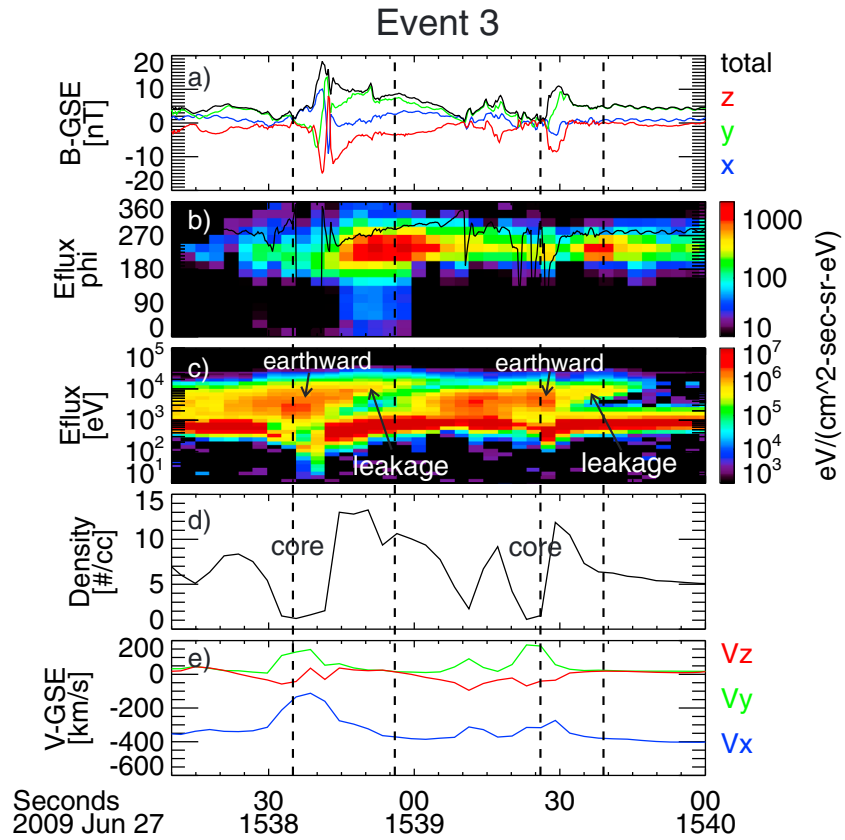
Figure 6. TH-B observations of Event 3. Same format as in Figures 1 and 4.

IMF had an almost zero X component upstream of both foreshock transients (Figure 6a). Thus, solar wind ions are only in the perpendicular direction (Figures 7c and 7g), and there are no sunward foreshock ions from the local bow shock. The energy dispersion is caused by increases in parallel speed of the secondary component for both transients. We note, in passing, that the IMF configuration and distribution evolution in this event are
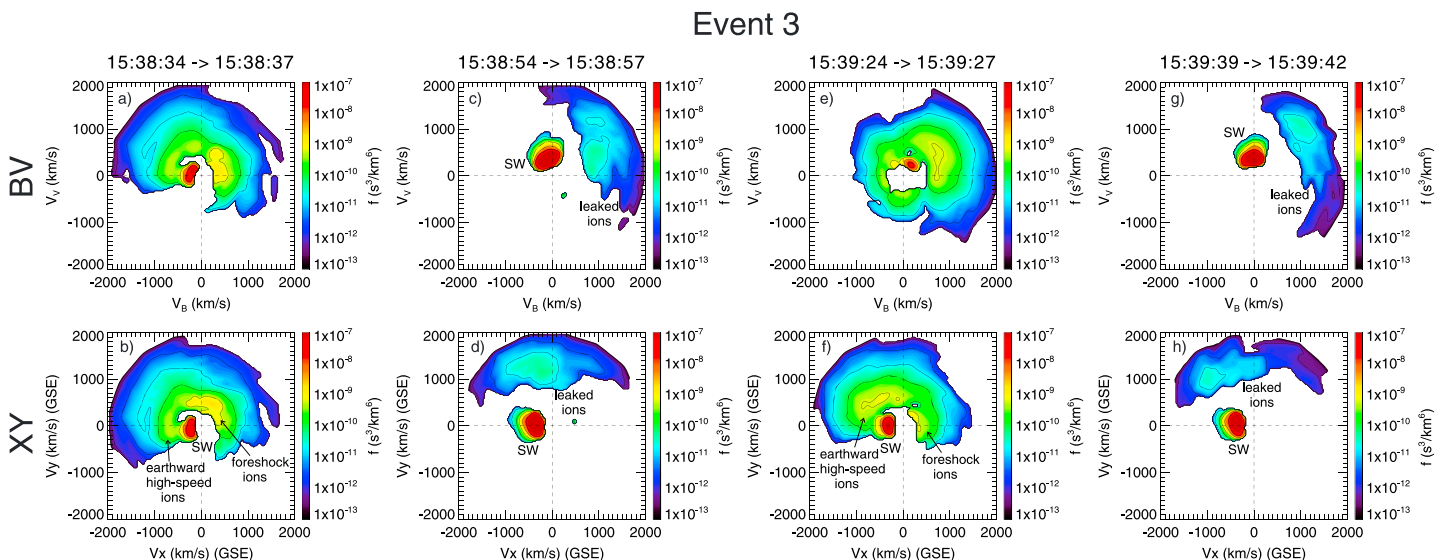

Figure 7. Ion distributions at four observation times (four columns correspond to four vertical dashed lines in Figure 4). Format same as in Figure 2.
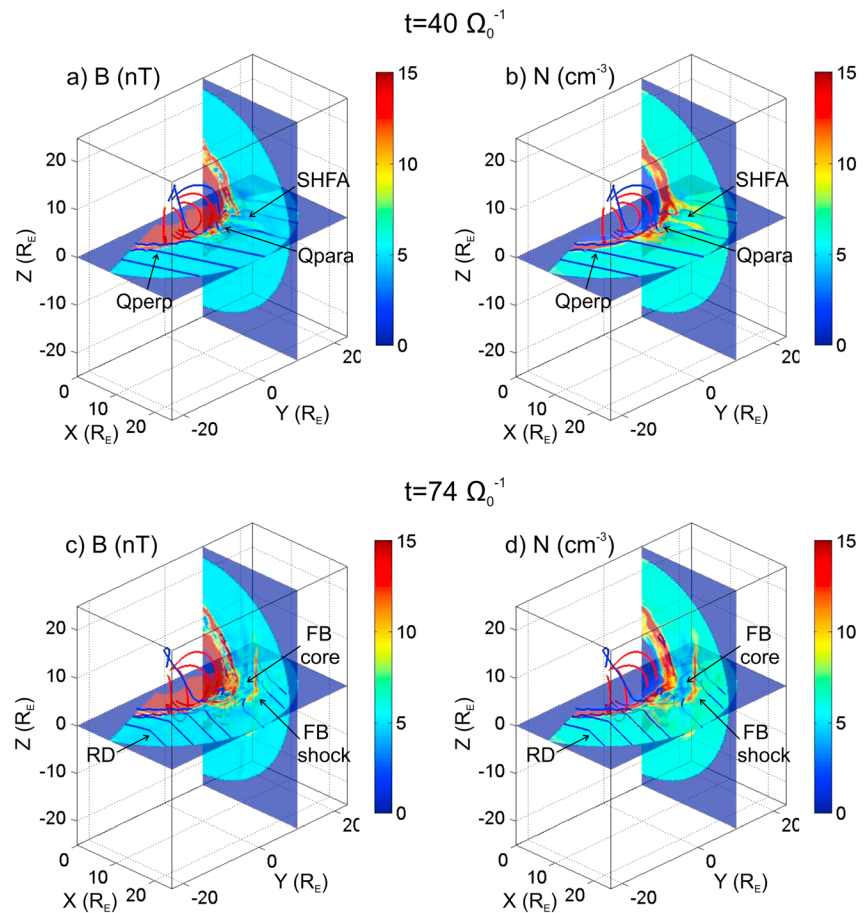
Figure 8. Three-dimensional global hybrid simulation results at time (a, b) $t = 40\ \Omega_0^{-1}$ to show the foreshock and (c, d) $t = 74\ \Omega_0^{-1}$ to show a fully formed FB. Contours of the magnetic field magnitude B(nT) (Figures 8a and 8c) and density N(cm^{-3}) (Figures 8b and 8d) in the XY ($Z = 0$) and XZ ($Y = 10\ R_E$) planes. Red lines indicate Earth's closed dipole field lines, and blue lines indicate IMF field lines. Quasi-parallel bow shock (Qpara), quasi-perpendicular bow shock (Qperp), spontaneous hot flow anomaly (SHFA), rotational discontinuity (RD), and foreshock bubble (FB core and FB shock) are labeled.

almost same as in the third event in Liu, Angelopoulos, and Hietala (2017), where leakage was also seen, except that those occurred on the other (the upstream) side of the HFA. As in our previous work, we argue that these ions are leaked from foreshock transients, propagating along the field line as they drift earthward. The observed dispersion is due to the fact that as the distance between the foreshock transient and the spacecraft increases, field-aligned ions with larger parallel speed but the same $E \times B$ drift speed can proceed farther along the field line.

4. Simulations

From the previous observations, we have shown that sunward foreshock ions in the cores of foreshock transients can be reflected by an earthward moving boundary and gain energy. To further confirm this, we employed a generic 3-D global hybrid simulation motivated by the characteristics epitomized by the 3 events presented herein represent the other 10 events in our database. Figure 8 shows our simulation result in an XY cut ($Z = 0$) and an XZ cut ($Y = 10\ R_E$, because the foreshock is in the first quadrant of the XY plane as IMF is $[-4.7, -1.7, 0]$ nT). Also shown in Movie S1 in the supporting information, after the bow shock forms the foreshock starts to develop upstream of quasi-parallel bow shock and is much more disturbed than quasi-perpendicular bow shock (Figures 8a and 8b). In the foreshock, spontaneous structures with large variation of density and field strength can be seen (including foreshock cavities, foreshock cavitons, and spontaneous hot flow anomalies). Later, a rotational discontinuity convects into the simulation domain. A foreshock
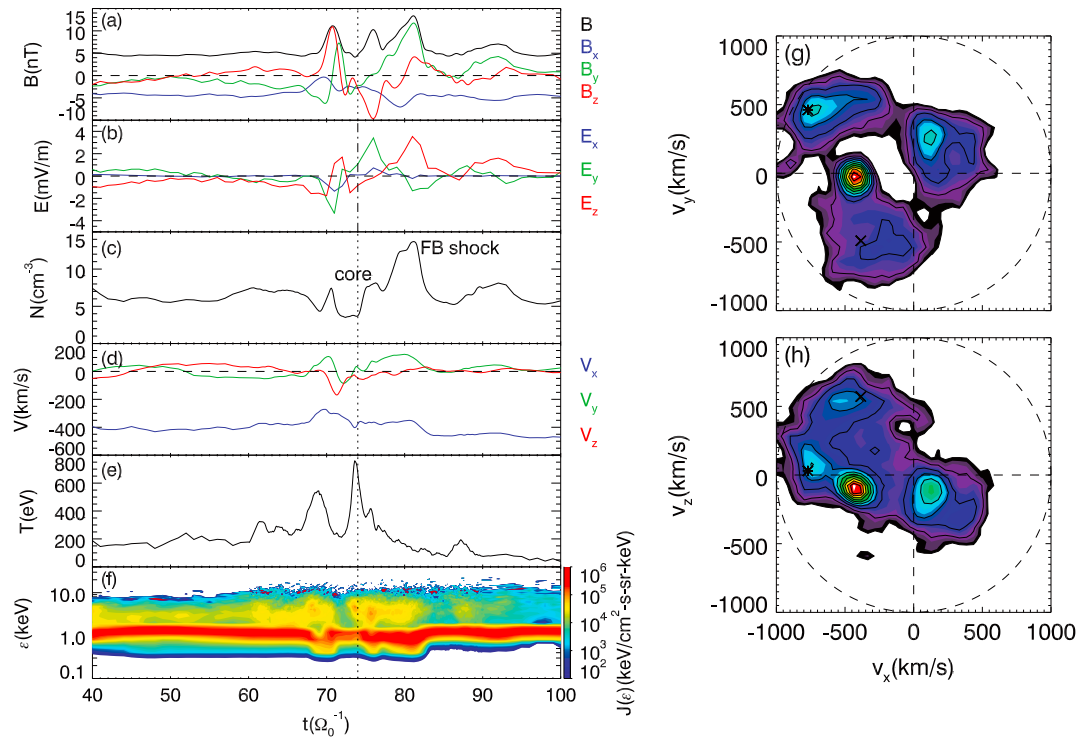
Figure 9. Virtual satellite observations at [13.2, 4.8, 0.0] R_E in the simulation for (a) magnetic field B (nT), (b) electric field E (mV/m), (c) ion density N (cm^{-3}), (d) ion flow velocity V (km/s), (e) ion temperature T (eV), and (f) ion energy flux $J(\varepsilon)$ (keV/(cm s sr keV)). Ion velocity distributions in the (g) (v_x, v_y) and (h) (v_x, v_z) planes at $t = 74 \, \Omega_0^{-1}$ (denoted by the vertical dotted line).

bubble (identified by its tenuous core bounded by a shock labeled in Figures 8c and 8d) forms upstream of the RD, grows larger and larger, and collides with the bow shock. The variation patterns of the magnetic field and density are quite similar. Our 3-D simulation is consistent with previous 2-D simulations by Omidi et al. (2010), except that the FB in our system has a finite shape in the YZ plane (Figure 8), leading to important constraints on how particles can evolve.

To compare more directly with observations, we put multiple virtual spacecraft in the first quadrant of the XY plane. Here we present the observation by one of these spacecraft at [13.2, 4.8, 0.0] R_E ($r = 14 \, R_E$, $\varphi = 70°$) as an example (Figure 9), because this spacecraft crosses the middle of the fully formed FB. Figure 9 reveals the classic signatures of a foreshock bubble with a hot, tenuous core bounded by a shock on its upstream side. Inside the core, there is an enhancement of ion energy flux at several keV (Figure 9f). To find the reason for the energy flux enhancement, we look at ion distributions (vertical dotted line in Figure 9) in the XY and XZ planes (Figures 9g and 9h). As in observations, there are three main components: the solar wind beam, a sunward foreshock ion beam, and an earthward high-speed component. The sunward foreshock ion speed is close to the solar wind speed; thus, the enhancement of ion energy flux at several keV corresponds to the most energetic earthward high-speed component, as in observations. Note that the earthward high-speed component has two beams, one mainly in the earthward direction with stronger flux, and the other one with a strong YZ component with weaker flux.

To understand the ion distributions, we trace each component in Figures 9g and 9h to obtain their trajectories. We first confirm that the solar wind beam is indeed directly from the solar wind (but decelerated; we will discuss this in section 5), and sunward ions are bow shock-reflected solar wind ions, that is, foreshock ions that enter the core (not shown here). What about earthward ions? Figure 10 shows representative ion trajectories corresponding to two earthward ion beams (star and cross in Figures 9g and 9h). As seen in Figures 10a–10d, both ions are originally solar wind ions. Then they are reflected by the bow shock and become foreshock ions. This process barely increases their energy (indicated by trajectory colors) because
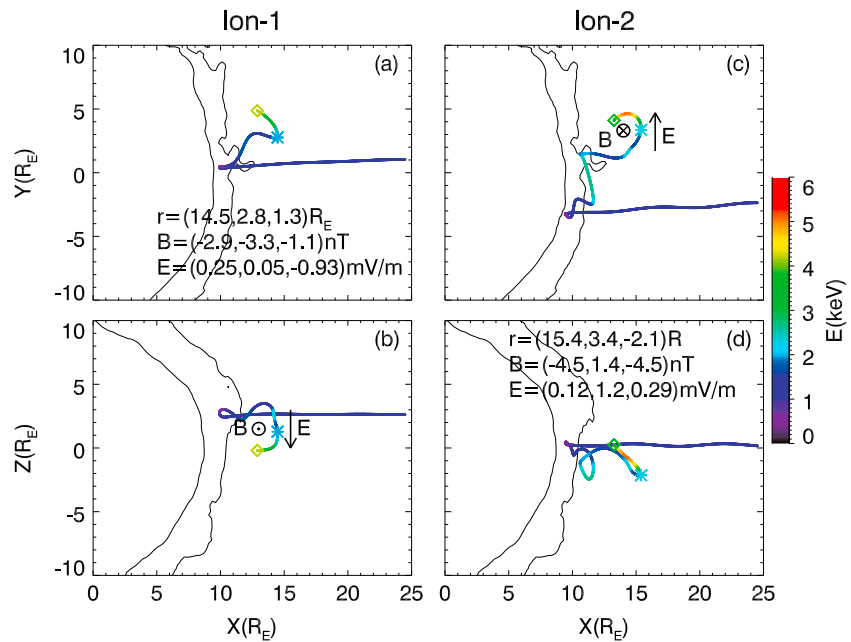
Figure 10. Two representative ion trajectories (projected in the *XY* and *XZ* planes) that are accelerated in the foreshock bubble. The color of the trajectories represents the energy of the ions. The black curves are the contours of number density at 11 cm^{-3} showing the locations of the magnetopause and bow shock mapped to the *XY* (*Z* = 0) and *XZ* (*Y* = 5R_E) planes. The prism indicates the virtual spacecraft. The asterisk indicates the reflection point with position (*r*), magnetic field (*B*), and electric field (*E*) listed.

the local bow shock is quasi-parallel. Then these sunward ions encounter the FB sheath and are reflected. Upon reflection the ions gain energy (from ~1–2 keV to 4.2 keV for ion-1 and to 3.7 keV for ion-2). (Movie S1 in the supporting information section shows the motion of traced ions even more clearly.) Therefore, our ion tracing results confirm our explanation of energization of earthward high-speed ions.

But how are ions reflected and why are there two beams? As seen in Figure 9a, there are two magnetic field peaks in the FB sheath: one mainly in the *Y* direction, and a second one mainly in the *Z* direction. In Figures 10a–10d, we label the magnetic and electric field directions at the time and location of reflection of each ion. As shown in Figures 10a and 10b (corresponding to star in Figures 9g and 9h), the local magnetic field has an enhanced B_y and electric field is dominated by E_z (we do not consider B_x as B_x does not affect V_x, but with a finite B_x the boundary is closer to a magnetic mirror than to a discontinuity). In Figure 10b, we see ions gyrate partially on the *XZ* plane along E_z back to the core. Ion-2 (cross in Figures 9g and 9h) is similar but reflected by the enhancement of B_z: ions partially gyrate on the *XY* plane along E_y (Figure 10c), although their reflection occurs at a different time for the two beams (corresponding to two different but well-formed magnetic structures within the FB). The calculated instant gyroradii of ion-1 and ion-2 using B_y and B_z at the reflection point (labeled in Figures 10a and 10d) are 1.98 R_E and 1.56 R_E, respectively, consistent with the ion trajectory shown in Figures 10b and 10c. Thus, both ion trajectories are consistent with our explanation of the reflection process from observations (Figures 2g and 2h): when ions in the core encounter the enhanced magnetic field in the *YZ* plane, they gyrate partially along the convection electric field (Earth frame) back to the core. Additionally, we see that the difference between the two beams is that they are reflected at different locations on the FB sheath with different magnetic field directions. Note that most of our observations and virtual spacecraft observations in simulations see only one earthward beam, probably because for ions reflected at different locations to reach the same point at the same time has rather low possibility.

In the observations, we saw that energetic ions in the core can leak out. To confirm this, we continued to trace these earthward high-speed ions after they reach the virtual spacecraft. (We do not show a full ion trajectory from solar wind to acceleration and then leakage, because details of acceleration and leakage can be seen more clearly in two separate figures.) Figure 11 shows two representative subsequent trajectories of these
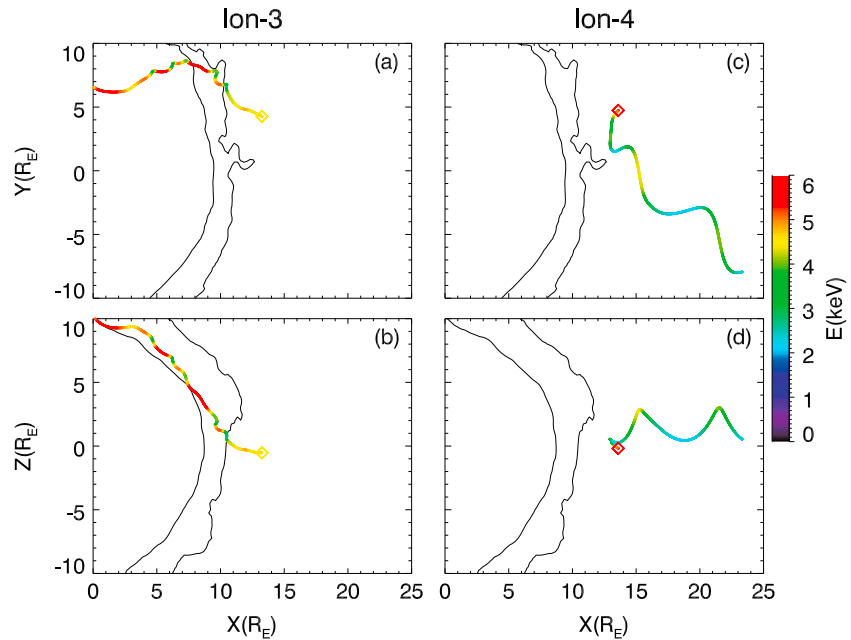
Figure 11. Two representative ion leakage trajectories after they have been accelerated inside the foreshock bubble. Same format as in Figure 10.

earthward high-speed ions. We see one traced ion directly leak downstream towards the bow shock, which is consistent with event 2 of our observations and similar to our sketch in Figure 3. The other one is reflected by the downstream boundary of the core and then exits the core on the upstream side, along the field line into the solar wind. This is more consistent with event 3 of our observations (although the field line direction is different in the observations). Thus, from simulations, we confirm that accelerated, energetic ions in the core can indeed leak out to both the downstream and upstream sides.

In our observations, we found that leakage can be accompanied by energy dispersion. In Figure 9, we can see dispersion, but only inside the core. At the other virtual spacecraft we observed energy dispersion on the downstream side of the core (not shown here). By analyzing ion distributions and the magnetic field direction, we found that the dispersion is caused by the local presence of B_z at the downstream boundary (this can also be seen in Figure 9a at $t = 71\ \Omega_0^{-1}$). Thus, some ions leaked downstream must gyrate prior to reaching the spacecraft. As the distance between the virtual spacecraft and FB decreases, these ions need smaller gyroradii or energy to reach the virtual spacecraft. This mechanism is similar to the first event in Liu, Angelopoulos, and Hietala (2017), in which $B_x = 0$ and ions leaked from an HFA need larger energy to gyrate towards the spacecraft as the HFA moves away from it.

5. Discussion

Our observation and simulation results show that ions in the core can be accelerated through reflection at the earthward moving boundary; that is, they execute at least one bounce from the bow shock to the foreshock transient boundary. But could there be multiple bounces? To answer this question, we need to know the fraction of reflection/leakage. Whether ions get reflected or leak out depends on how further ions penetrate the boundary. In our reflection model (Figure 3), we simplify the field direction in the boundary to be along the boundary surface. Thus, the maximum distance that ions penetrate is $R - R \cdot \sin \varphi$, where R is ion gyroradius and φ is the initial gyrophase when ions enter the boundary (from $-\pi/2$ to $\pi/2$). The flux fraction of leakage assuming isotropic distribution with certain speed v is $(2/\pi) \int_{\theta_c}^{\pi/2} \sin \theta \sin \theta \, d\theta \int_{-\pi/2}^{\varphi_c} \cos \varphi \, d\varphi$, where θ is the initial pitch angle, $\sin \theta_c = Bqd/mv$, and $\sin \varphi_c = 1 - \sin \theta_c / \sin \theta$. When $\sin \theta_c = Bqd/mv \leq 1$ (otherwise there is no leakage), we have the flux fraction of leakage as $1 - 2\theta_c/\pi$. We see that larger ion energy, smaller field strength, and smaller boundary thickness can result in more leakage. For example, when $B = 10$ nT,

d = 1000 km, and particle energy is 10 keV, the flux fraction of leakage is ~51%. This means that while multiple bounces are still possible, their probability becomes lower and lower as the particle energy increases. In the simulation, we do see 2–3 bounces accelerating ions to tens of keV (e.g., Movie S1c), but the flux is very low (limited by the number of particles in the 3-D simulations—with more particles there could be even more bounces observed in the simulation resulting in even higher energies). In the future, we could further investigate the model of multiple bounces by calculating theoretical spectra and comparing them with observations and simulations.

Next, we discuss the potential impact of ion acceleration by foreshock transients. After the ions are accelerated, some of them leak downstream into the magnetosheath and move toward high latitudes (e.g., Figures 11a and 11b). These ions could later enter the magnetosphere through the cusp, as shown in the study by Lin et al. (2007), affecting the magnetosphere-ionosphere system. In fact, from simulations we see some energetic ions that enter the magnetosheath can also be ejected out into the solar wind later, becoming foreshock ions again, but now with much higher energy than typical foreshock ions. In Figures 11c and 11d, we see a case of how energetic ions can also directly leak upstream, contributing to foreshock ions. The potential geoeffectiveness of foreshock transient-accelerated particles requires further investigation.

The quasi-parallel bow shock is widely considered as an ineffective particle accelerator compared to the quasi-perpendicular shock (smaller acceleration rates (e.g., Lee et al., 2012); this is consistent with our observations and simulations showing that the foreshock ion speed is quite close to the solar wind speed (e.g., Figures 2, 5, and 9)). However, when foreshock transients form upstream of the quasi-parallel shock, they can help quasi-parallel shock to provide very energetic ions, which could be scattered to become diffuse foreshock ions. The source of diffuse foreshock ions is still debated. This study, along with a previous one (Liu, Hietala, et al., 2016) revealing solar wind ion acceleration at the new foreshock of an FB shock, indicates that foreshock transients, though formed from foreshock ions themselves, may in turn become one of the sources of diffuse foreshock ions.

Ion acceleration inside foreshock transients again indicates that foreshock transients could be a preaccelerator for parent bow shock diffusive shock acceleration, as suggested by Liu, Hietala, et al. (2016) and Wilson et al. (2016). Additionally, from Movie S1, we see that before the formation of FB, many spontaneous foreshock transients formed. From particle tracing in such complex but self-consistent fields, we see that some traced ions can experience acceleration by repeated reflections between the bow shock and these spontaneous structures. This implies that foreshock transients may also be an integral part of the parent shock's ion diffusive shock acceleration. The possible role of foreshock transients in parent shock acceleration needs further study in future.

From ion energy spectra in observations and simulations (Figures 1c, 1e, 4c, 4e, 6c, 6e, 9d, and 9f), we notice another common characteristic: continuous deceleration of solar wind speed in the core. From an MHD perspective, concentration and thermalization of foreshock ions by the driver discontinuity can result in a local enhancement in thermal pressure. Such thermal pressure can then decelerate solar wind ions, in other words, expand and push back cold solar wind ions in the solar wind frame. The expansion requires the divergence of velocity to be positive. In the solar wind frame, continuous deceleration of solar wind speed becomes continuous acceleration of expansion speed along the sunward direction, the expansion direction, resulting in positive divergence of velocity (which is the reason for the density decrease inside the core). Thus, the gradual deceleration of the solar wind speed is a sign of foreshock transient expansion in the sunward direction. And similarly, the expansion in other directions can result in continuous deflection of solar wind direction.

In this study, an FB driven by a rotational discontinuity is simulated as an example to compare with observations and visualize the bouncing process. Other types of foreshock transients with compressional boundaries (including HFAs, SHFAs, and foreshock cavities) can have similar process with different details. For example, in the simulation before the arrival of FB, some ions bounce between the bow shock and multiple spontaneous foreshock transients (see Movie S1). Additionally, because HFAs move along the bow shock surface in *YZ* direction, ions reflected by HFA's upstream boundary could also have strong *YZ* component (e.g., Figure 7f). In future, more simulations could be applied to confirm these details.

In this study, we show one ion acceleration mechanism inside foreshock transients that can explain a moderate subset of our events (63 out of 247). In other events, there could also be ion acceleration, but it is hard to identify. For example, in some events, ions are so diffuse that we cannot distinguish any of their components.

Other possible acceleration mechanisms, including wave-particle interactions, need to be further investigated in the future.

6. Summary and Conclusions

From observations, we show that in a moderate subset of events (63 of 247 events), there is ion energy flux enhancement in foreshock transients' cores at several keV to tens of keV corresponding to earthward moving ions. By analyzing ion distributions and the magnetic field direction at the FB sheath, we reveal that those earthward high-speed ions are reflected and accelerated at the earthward moving foreshock transient boundary through partial gyration along the convection electric field. We show that those energetic ions can leak out of the core into the surroundings, which is consistent with our previous study (Liu, Lu, et al., 2017). To further confirm observation results, we conduct 3-D global hybrid simulations. We show similar ion energy flux enhancement up to several keV corresponding to earthward high-speed ions. By using particle tracing, we confirm that those ions are indeed reflected and accelerated by the earthward moving boundary through partial gyration along an electric field. We also confirm that those ions can leak out both downstream and upstream. Therefore, we conclude that foreshock transients can indeed accelerate ions inside them and that one acceleration mechanism is reflection at an earthward moving boundary.

This study, along with other recent observations (e.g., Liu, Hietala, et al., 2016; Liu, Angelopoulos, & Hietala, 2017; Liu, Angelopoulos, Hietala, & Wilson, 2017; Liu, Lu, et al., 2017; Wilson et al., 2016), demonstrates foreshock transients' ability to accelerate particles, implying that they have an important role in shock acceleration like providing a source for diffusive shock acceleration and repopulating foreshock ions, and potentially contributing to enhanced magnetospheric fluxes. These topics deserve more attention and multipoint studies in the future.

References

Angelopoulos, V. (2008). The THEMIS mission. *Space Science Reviews*, *141*(1-4), 5–34. https://doi.org/10.1007/s11214-008-9336-1

Archer, M. O., Turner, D. L., Eastwood, J. P., Horbury, T. S., & Schwartz, S. J. (2014). The role of pressure gradients in driving sunward magnetosheath flows and magnetopause motion. *Journal of Geophysical Research: Space Physics*, *119*, 8117–8125. https://doi.org/10.1002/2014JA020342

Archer, M. O., Turner, D. L., Eastwood, J. P., Schwartz, S. J., & Horbury, T. S. (2015). Global impacts of a foreshock bubble: Magnetosheath, magnetopause and ground-based observations. *Planetary and Space Science*, *106*, 56–66. https://doi.org/10.1016/j.pss.2014.11.026

Auster, H. U., Glassmeier, K. H., Magnes, W., Aydogar, O., Baumjohann, W., Constantinescu, D., … Wiedemann, M. (2008). The THEMIS fluxgate magnetometer. *Space Science Reviews*, *141*(1-4), 235–264. https://doi.org/10.1007/s11214-008-9365-9

Blanco-Cano, X., Kajdič, P., Omidi, N., & Russell, C. T. (2011). Foreshock cavitons for different interplanetary magnetic field geometries: Simulations and observations. *Journal of Geophysical Research*, *116*, A09101. https://doi.org/10.1029/2010JA016413

Burgess, D., Möbius, E., & Scholer, M. (2012). Ion acceleration at the Earth's bow shock. *Space Science Reviews*, *173*(1-4), 5–47. https://doi.org/10.1007/s11214-012-9901-5

Caprioli, D., Pop, A.-R., & Spitkovsky, A. (2015). Simulations and theory of ion injection at non-relativistic collisionless shocks. *The Astrophysical Journal*, *798*(2), L28. https://doi.org/10.1088/2041-8205/798/2/L28

Eastwood, J. P., Lucek, E. A., Mazelle, C., Meziane, K., Narita, Y., Pickett, J., & Treumann, R. A. (2005). The foreshock. *Space Science Reviews*, *118*(1-4), 41–94. https://doi.org/10.1007/s11214-005-3824-3

Jokipii, J. R. (1987). Rate of energy gain and maximum energy in diffusive shock acceleration. *The Astrophysical Journal*, *313*, 842. https://doi.org/10.1086/165022

Kis, A., Agapitov, O., Krasnoselskikh, V., Khotyaintsev, Y. V., Dandouras, I., Lemperger, I., & Wesztergom, V. (2013). Gyrosurfing acceleration of ions in front of earth's quasi-parallel bow shock. *The Astrophysical Journal*, *771*(1), 4. https://doi.org/10.1088/0004-637X/771/1/4

Lee, M. A., Mewaldt, R. A., & Giacalone, J. (2012). Shock acceleration of ions in the heliosphere. *Space Science Reviews*, *173*(1-4), 247–281. https://doi.org/10.1007/s11214-012-9932-y

Lin, Y. (2002). Global hybrid simulation of hot flow anomalies near the bow shock and in the magnetosheath. *Planetary and Space Science*, *50*(5-6), 577–591. https://doi.org/10.1016/S0032-0633(02)00037-5

Lin, Y. (2003). Global-scale simulation of foreshock structures at the quasi-parallel bow shock. *Journal of Geophysical Research*, *108*(A11), 1390. https://doi.org/10.1029/2003JA009991

Lin, Y., & Wang, X. Y. (2005). Three-dimensional global hybrid simulation of dayside dynamics associated with the quasi-parallel bow shock. *Journal of Geophysical Research*, *110*, A12216. https://doi.org/10.1029/2005JA011243

Lin, Y., Wang, X. Y., & Chang, S.-W. (2007). Connection between bow shock and cusp energetic ions. *Geophysical Research Letters*, *34*, L11107. https://doi.org/10.1029/2007GL030038

Lin, Y., Wang, X. Y., Lu, S., Perez, J. D., & Lu, Q. (2014). Investigation of storm time magnetotail and ion injection using three-dimensional global hybrid simulation. *Journal of Geophysical Research: Space Physics*, *119*, 7413–7432. https://doi.org/10.1002/2014JA020005

Liu, T. Z., Angelopoulos, V., & Hietala, H. (2017). Energetic ion leakage from foreshock transient cores. *Journal of Geophysical Research: Space Physics*, *122*, 7209–7225. https://doi.org/10.1002/2017JA024257

Liu, T. Z., Angelopoulos, V., Hietala, H., & Wilson, L. B. III (2017). Statistical study of particle acceleration in the core of foreshock transients. *Journal of Geophysical Research: Space Physics*, *122*, 7197–7208. https://doi.org/10.1002/2017JA024043

Liu, T. Z., Hietala, H., Angelopoulos, V., & Turner, D. L. (2016). Observations of a new foreshock region upstream of a foreshock bubble's shock. *Geophysical Research Letters*, *43*, 4708–4715. https://doi.org/10.1002/2016GL068984

Liu, T. Z., Lu, S., Angelopoulos, V., Hietala, H., & Wilson, L. B. III (2017). Fermi acceleration of electrons inside foreshock transient cores. *Journal of Geophysical Research: Space Physics*, *122*, 9248–9263. https://doi.org/10.1002/2017JA024480

Liu, T. Z., Turner, D. L., Angelopoulos, V., & Omidi, N. (2016). Multipoint observations of the structure and evolution of foreshock bubbles and their relation to hot flow anomalies. *Journal of Geophysical Research: Space Physics*, *121*, 5489–5509. https://doi.org/10.1002/2016JA022461

Liu, Z., Turner, D. L., Angelopoulos, V., & Omidi, N. (2015). THEMIS observations of tangential discontinuity-driven foreshock bubbles. *Geophysical Research Letters*, *42*, 7860–7866. https://doi.org/10.1002/2015GL065842

McFadden, J. P., Carlson, C. W., Larson, D., Angelopoulos, V., Ludlam, M., Abiad, R., … Marckwordt, M. (2008). The THEMIS ESA plasma instrument and in-flight calibration. *Space Science Reviews*, *141*(1-4), 277–302. https://doi.org/10.1007/s11214-008-9440-2

Omidi, N., Eastwood, J. P., & Sibeck, D. G. (2010). Foreshock bubbles and their global magnetospheric impacts. *Journal of Geophysical Research*, *115*, A06204. https://doi.org/10.1029/2009JA014828

Omidi, N., & Sibeck, D. G. (2007). Formation of hot flow anomalies and solitary shocks. *Journal of Geophysical Research*, *112*, A10203. https://doi.org/10.1029/2006JA011663

Omidi, N., Zhang, H., Sibeck, D., & Turner, D. (2013). Spontaneous hot flow anomalies at quasi-parallel shocks: 2. Hybrid simulations. *Journal of Geophysical Research*, *118*, 173–180. https://doi.org/10.1029/2012JA018099

Schwartz, S. J. (1998). Shock and discontinuity normal, Mach numbers, and related parameters. In G. Paschmann, & P. W. Daly (Eds.), *Analysis methods for multi-spacecraft data* (pp. 249–270). Noord- wijk, Netherlands: ESA Publications Division.

Schwartz, S. J., Chaloner, C. P., Christiansen, P. J., Coates, A. J., Hall, D. S., Johnstone, A. D., … Woolliscroft, L. J. C. (1985). An active current sheet in the solar wind. *Nature*, *318*(6043), 269–271. https://doi.org/10.1038/318269a0

Schwartz, S. J., Sibeck, D., Wilber, M., Meziane, K., & Horbury, T. S. (2006). Kinetic aspects of foreshock cavities. *Geophysical Research Letters*, *33*, L12103. https://doi.org/10.1029/2005GL025612

Sibeck, D. G., & Angelopoulos, V. (2008). THEMIS science objectives and mission phases. *Space Science Reviews*, *141*(1-4), 35–59. https://doi.org/10.1007/s11214-008-9393-5

Sibeck, D. G., Borodkova, N. L., Schwartz, S. J., Owen, C. J., Kessel, R., Kokubun, S., … Zastenker, G. N. (1999). Comprehensive study of the magnetospheric response to a hot flow anomaly. *Journal of Geophysical Research*, *104*(A3), 4577–4593. https://doi.org/10.1029/1998JA900021

Sibeck, D. G., Phan, T. D., Lin, R. P., Lepping, R. P., & Szabo, A. (2002). Wind 556 observations of foreshock cavities: A case study. *Journal of Geophysical Research*, *107*(A10), 1271. https://doi.org/10.1029/2001JA007539

Sundberg, T., Christopher, T. H., Burgess, D., & Christian, X. M. (2016). Ion acceleration at the quasi-parallel bow shock: Decoding the signature of injection. *APJ*, *820*(1), 21. https://doi.org/10.3847/0004-637X/820/1/21

Tan, B., Lin, Y., Perez, J. D., & Wang, X. Y. (2011). Global-scale hybrid simulation of dayside magnetic reconnection under southward IMF: Structure and evolution of reconnection. *Journal of Geophysical Research*, *116*, A02206. https://doi.org/10.1029/2010JA015580

Turner, D. L., Omidi, N., Sibeck, D. G., & Angelopoulos, V. (2013). First observations of foreshock bubbles upstream of Earth's bow shock: Characteristics and comparisons to HFAs. *Journal of Geophysical Research: Space Physics*, *118*, 1552–1570. https://doi.org/10.1002/jgra.50198

Wilson, L. B. III, Koval, A., Sibeck, D. G., Szabo, A., Cattell, C. A., Kasper, J. C., … Wilber, M. (2013). Shocklets, SLAMS, and field-aligned ion beams in the terrestrial foreshock. *Journal of Geophysical Research: Space Physics*, *118*, 957–966. https://doi.org/10.1029/2012JA018186

Wilson, L. B. I. I. I., Sibeck, D. G., Turner, D. L., Osmane, A., Caprioli, D., & Angelopoulos, V. (2016). Relativistic electrons produced by foreshock disturbances observed upstream of Earth's bow shock. *Physical Review Letters*, *117*(21), 215101. https://doi.org/10.1103/PhysRevLett.117.215101

Zhang, H., Sibeck, D. G., Zong, Q.-G., Omidi, N., Turner, D., & Clausen, L. B. N. (2013). Spontaneous hot flow anomalies at quasi-parallel shocks: 1. Observations. *Journal of Geophysical Research: Space Physics*, *118*, 3357–3363. https://doi.org/10.1002/jgra.50376